의학박사 학위논문

Relationship Between K_{trans} and K_1 with Simultaneous *versus* Separate MR/PET in Rabbits with VX2 Tumors

토끼 VX2 종양의 MR/PET 영상을 동시 촬영했을 때와 분리 촬영했을 때의 K_{trans} 와 K_1 관계 비교 연구

2017 년 7 월

서울대학교 대학원

의학과 영상의학 전공

이 경 희

토끼 VX2 종양의 MR/PET 영상을 동시 촬영했을 때와 분리 촬영했을 때의 K_{trans} 와 K_1 관계 비교 연구

지도교수 구 진 모

이 논문을 의학박사 학위논문으로 제출함

2017 년 4 월

서울대학교 대학원

의학과 영상의학 전공

이 경 희

이경희의 의학박사 학위논문을 인준함

2017 년 7 월

위 원 장	문우경	(인)
부위원장	구진모	(인)
위 원	강건욱	(인)
위 원	이정민	(인)
위 원	정명진	(인)

ABSTRACT

Relationship Between K_{trans} and K_1 with Simultaneous *versus* Separate MR/PET in Rabbits with VX2 Tumors

Kyung Hee Lee

The Department of Radiology

The Graduate school

Seoul National University

Introduction: The purpose of this experimental study was to compare the relationship of K_{trans} from DCE-MRI and K_1 from dynamic ^{13}N-NH_3-PET between simultaneous and separate MR/PET acquisition in the VX2 rabbit carcinoma model.

Methods: Eight rabbits underwent MR/PET examination simultaneously and separately, 14 and 15 days after VX2 tumor implantation at the left paravertebral muscle. The K_{trans} and K_1 values were estimated using an in-house software program. The

relationships between K_{trans} and K_1 were analyzed using Pearson's correlation coefficients and linear/nonlinear regression function.

Results: This study finally included five rabbits. Assuming a linear relationship, K_{trans} and K_1 exhibited moderate positive correlations with both simultaneous ($r = 0.54–0.57$) and separate ($r = 0.53–0.69$) imaging. However, while the K_{trans} and K_1 from separate imaging were linearly correlated, those from simultaneous imaging exhibited a nonlinear relationship. The amount of change in K_1 associated with a unit increase in K_{trans} varied depending on K_{trans} values.

Conclusions: The relationship between K_{trans} and K_1 was different between simultaneous and separate MR/PET acquisition. The relationship between K_{trans} and K_1 may be mis-interpreted with separate MR and PET acquisition.

Keywords: MR/PET, dynamic contrast enhanced-MRI, $^{13}N-NH_3$ PET, perfusion parameter, rabbit

Student number: 2013-30559

Table of Contents

List of Tables

List of Figure

INTRODUCTION

With the recently introduced hybrid MR/PET machine, MR and PET images can be obtained simultaneously with perfect temporal and much improved spatial co-registration (1-3). MR imaging has high spatial resolution, high contrast resolution and enables diverse functional imaging while PET imaging can visualize molecular functional information including metabolic activity. With hybrid MR/PET machine, these advantages of MR and PET imaging can be combined to enable better assessment of physiologic and pathologic state in vivo with much improved workflow efficiency. Moreover, the simultaneity of hybrid MR/PET systems offers several advantages over separate MR and PET and PET/computed tomography (CT) (4, 5), including precise patient alignment, recording of dynamic phenomena, tissue information under identical physiologic state from both modalities, and better localization of PET signals in soft tissues (6). In terms of patient alignment, a previous study reported better alignment quality with simultaneous MR/PET than with retrospective fusion of MR and PET data (7). However, there has been no study that evaluated the simultaneity of hybrid MR/PET systems based on functional information.

Dynamic contrast-enhanced magnetic resonance imaging (DCE-MRI) perfusion parameters are widely used for assessment of treatment response to anti-angiogenic drugs in both preclinical studies and clinical trials (8, 9). The main advantages of DCE-MRI are its high spatial resolution and nonuse of ionizing radiation (10, 11). However, absolute quantification of flow is difficult because there is no linear relationship between signal intensity and gadolinium (Gd) concentration, and interpretation of DCE-MRI perfusion parameter is complicated. The transfer constant, K_{trans}, has several physiologic interpretations, depending on the balance between capillary permeability and blood flow in the tissue of interest. On the other hand, dynamic $^{13}N-NH_3$ positron emission tomography (PET) perfusion parameter, K_1, is more straightforward, because K_1 primarily reflects blood flow owing to high extraction fraction of $^{13}N-NH_3$ (12, 13). Clarifying the relationship between K_{trans} and K_1 might enhance our understanding of tumor angiogenesis and vascular permeability (14). While dynamic $^{13}N-NH_3$ PET has been clinically utilized in myocardial perfusion imaging (12, 13), its utility in tumor imaging is under-investigated. However, several reports involving this technique have demonstrated promising results (15-18) in the diagnosis of

brain tumors and fibrosarcomas using qualitative or semi-quantitative analysis.

The purpose of this study was to compare the relationship of K_{trans} from DCE-MRI and K_1 from dynamic ^{13}N-NH_3-PET between simultaneous and separate MR/PET acquisition in the VX2 rabbit carcinoma model.

MATERIALS AND METHODS

This study was approved by the Animal Care and Use Committee in our institution (Permit number: 13-0394-C1A1(3)).

Animal Model

New Zealand White rabbits weighing 3.0-3.5 kg, were selected for this study animal model. For the pilot study, four rabbits were included, and for the main study, eight rabbits were included. The rabbit VX2 tumor model was chosen for the following reasons; (a) it is a reliable transplantable tumor model that has not been well established in large animals (19), (b) rodents are too small in size to obtain reliable perfusion parameters with MR/PET, (c) many previous studies have employed the rabbit VX2 tumor model for DCE-MR imaging (20, 21), and (d) the preclinical animal

experimental center of our institute periodically inoculates VX2 cells into the thigh muscles of New Zealand White rabbits to maintain *in vivo* passages of VX2 cells, thus making the cells easily accessible for this study.

Prior to tumor implantation, animals were sedated by intravenous injection of 5 mg/kg of a 1:1 combination of tiletamine hydrochloride and zolazepam (Zoletil; Virbac, Carros, France) and xylazine hydrochloride (Rompun 2%; Bayer Korea, Seoul, Korea). After anesthesia and shaving of the paravertebral area, 0.2 ml of a suspension of finely minced fresh VX2 tumor was implanted in the left paravertebral muscle at the level of heart, using 16-gauge Medicut needles under ultrasonographic guidance. The heart was required to be within the scan range in order to measure the arterial input function of dynamic MR/PET. One week after tumor implantation, ultrasonography examination was performed by one radiologist (K.H.L.) under the anesthesia to determine whether tumor implantation was successful. Two weeks after tumor implantation, the VX2 tumors were expected to be approximately 2 cm along the longest dimension, appropriate for tumor perfusion imaging. Each rabbit was subjected to MR/PET (Biograph mMR, Siemens Healthcare, Erlangen, Germany) on two successive days, 14 days after tumor implantation. All efforts were made to minimize

the suffering of animals during tumor implantation and MR/PET.

MR/PET

Rabbits were anesthetized, and a 20-gauge intra-venous cannula (Medicut) was inserted into the right marginal ear vein before the start of MR/PET. The MR/PET acquisition protocol is illustrated in **Figure 1**. Simultaneous MR and PET image acquisition was performed 14 days after tumor implantation. For dynamic MR/PET, 0.2 mmol/kg gadoterate meglumine (Dotarem; Guerbet, Bloomington, IN, USA) and 111 MBq $^{13}N-NH_3$ were hand injected simultaneously using three-way stopcocks, followed by 8 ml saline chaser. The total injection volume of MR and PET contrast media was made up to 2 ml by dilution with normal saline to maintain uniform concentration of MR contrast media at every examination. Contrast media was injected slowly over a 30-s duration. The total scan time was approximately 25 min. Separate MRI and PET image acquisition was performed 15 days after tumor implantation. After completion of PET, the rabbits were removed from the MR/PET scanner and placed back inside the scanner approximately 60 minutes later. The animals were positioned on their back at the same level as the MRI table. The dose, volume and method of

injection of injection of MR and PET contrast media were maintained the same between simultaneous and separate imaging. However, during separate MR and PET, 2ml normal saline was hand injected simultaneously as the control. The total examination time for separate imaging was approximately 40 min. Scanning parameters for MRI and PET were maintained the same for simultaneous and separate imaging, as described below.

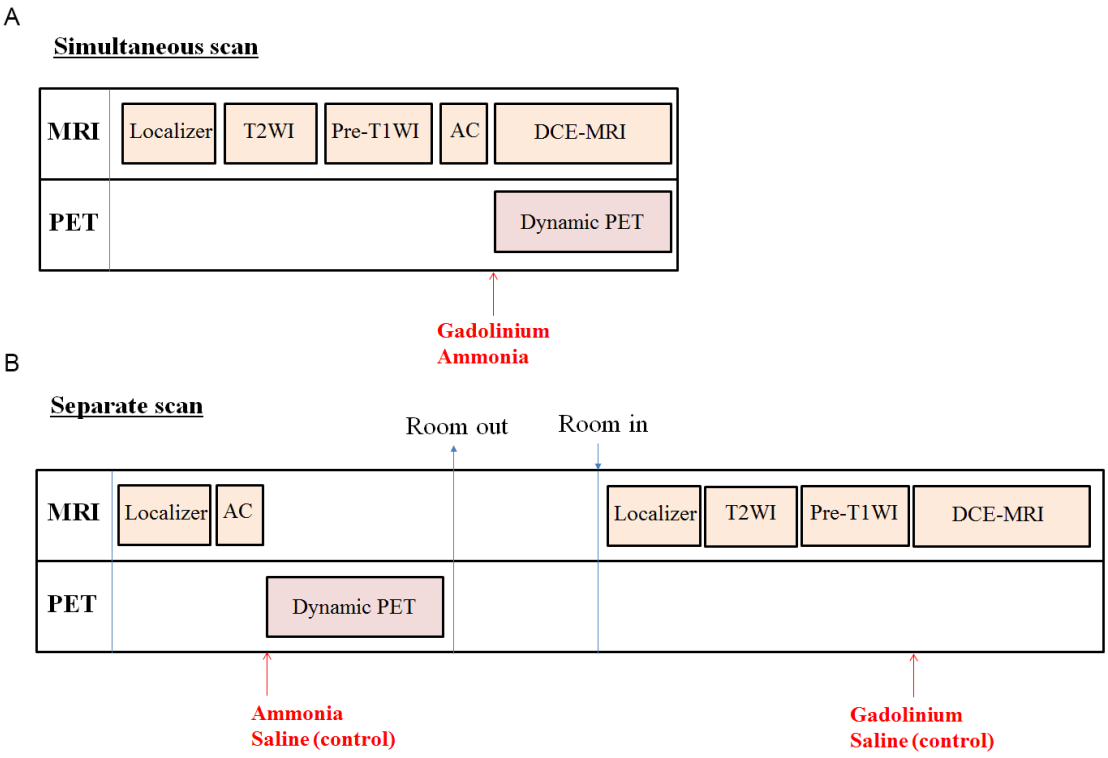

Figure 1. Schematic drawing of the MR/PET acquisition protocol.

Schematic drawing of the MR/PET acquisition protocol. (A) Simultaneous MR/PET acquisition and (B) Separate MR and PET acquisition, 14 and 15 days after tumor implantation, respectively.

Pilot Study

To set-up MR/PET protocol, animal model and to train research assistants, a pilot study was performed using four rabbits. Two research assistants helped in animal care and transportation. VX2 tumor was implanted in the left paravertebral muscle of each rabbit. One week after tumor implantation, successful growth of VX2 tumors was confirmed in all four rabbits on ultrasonography. Four rabbits underwent MR/PET examination, 14 days after tumor implantation. In one rabbit, tumor was located at the posterior mediastinum. Therefore, efforts were made to locate the needle tip in the paravertebral muscle area during tumor implantation in the main study. Three rabbits died from air-embolism during the simultaneous 10-min dynamic MR/PET examination. It was assumed that air inside the three-way connectors might have caused air-embolism. Therefore, efforts were made to minimize the air inside the three-way connectors through flushing saline in the main study. The remaining one rabbit successfully underwent MR/PET and were sacrificed after the second MR/PET imaging session by intravenous injection of 5 ml potassium chloride while under deep anesthesia. However, this rabbit was not included for the analysis of main study because the DCE-MRI parameters had been adjusted in the main experiment.

DCE-MRI parameters

All MR images were acquired using dedicated head and body coils approved for MR/PET at the same time. T2-weighted imaging (T2WI) was performed with the following parameters: repetition time/echo time (TR/TE), 4100/87 ms; matrix size, 128 x 128; slice thickness, 3 mm; and field of view (FOV), 130 x 130 mm. Pre-T1-weighted (T1W) images were acquired with a gradient echo sequence (GRE) called weighted volumetric interpolated breath-hold examination (VIBE) at each of the four flip angles for T1 mapping using the following parameters: TR/TE 4.4/1.1 ms; flip angles (α=2°, 5°, 10° and 15°); matrix size 128 x 128; slice thickness 3 mm; number of slices 20; and 130 x 130 mm. Using the VIBE sequence, DCE-MR images were obtained at 5 s of temporal resolution with the following parameters: TR/TE, 3.5/1.5 ms; flip angles (α=11°); matrix size 128 x 128; slice thickness, 3 mm; number of slices, 20; and FOV, 130 x 130 mm. The total acquisition time of dynamic scan including the first six phases of pre-contrast images was 10 min.

Dynamic $^{13}N-NH_3$ PET parameters

We planned on examining two rabbits per synthesis of $^{13}N-$

NH_3 (up to 200mCi/cassette). Since the radioactivity of $^{13}N-NH_3$ decreases at the time of second injection, the volume of $^{13}N-NH_3$ that corresponds to 111 MBq is greater than that at the time of first injection. Theoretically, if 200 mCi of $^{13}N-NH_3$ can be synthesized per one cassette, and the volume of $^{13}N-NH_3$ that corresponds to 111 MBq at the time of second injection would be 1.2ml if the time interval between the MR/PET examination was 40 min. However, practically, the synthesis of $^{13}N-NH_3$ does not occur in 100%, so that synthesized $^{13}N-NH_3$ is usually less than 200 mCi. Therefore, the injection volume of contrast media was set as 2ml to consider the practically synthesized amount of $^{13}N-NH_3$ per one cassette.

An approximately 20-s T1W Dixon GRE image in the coronal plane was first acquired for attenuation correction. Then, the emission protocol of a 10-min dynamic scan (6 x 5 s [precontrast]); 12 x 5 s; 3 x 10 s; 6 x 30 s; 2 x 60 s; and 1 x 180 s) was implemented. The 30-s precontrast phase was included to maintain uniformity between dynamic $^{13}N-NH_3$ PET and DCE-MRI. Dynamic PET images were reconstructed by point spread function modeling.

Image Analysis

One board-certified radiologist (K.H.L.), with four years of experience after board certification, measured the diameter of whole tumor, that of necrotic area, and the proportion of necrotic area on delayed phase images from simultaneous and separate examination in each rabbit, respectively. In addition, the same radiologist manually drew region-of-interests (ROIs) on the left ventricle and tumors on DCE-MR images using MRIcro (http://www.sph.sc.edu/comd/rorden/mricro.html). To derive individual arterial input function (AIF) curves, ROIs were drawn in the left ventricle in three or four different image slices in the peak arterial enhancement phase of imaging. The radiologist also manually drew ROIs on tumors by outlining the entire tumor boundary as delineated by contrast enhancement in all involved MR slices containing the tumor in one of the delayed phases in which tumor was appropriately enhanced.

In-house software program development

Two commercially available software programs, Tissue 4D and Nordic, did not provide the function of parameter calculation on the basis of the individual AIF with perfusion map on voxel-level. Therefore, we developed an in-house software program using customized matrix laboratory (MATLAB) scripts (The Mathworks

Inc., Natick, MA, USA) to generate K_{trans} and K_1 maps on ROI- and voxel-level from DCE-MRI and $^{13}N-NH_3$ PET using individual AIF curves. For simultaneous image acquisition, the MR and PET data were resampled to match the image coordinates and dimensions. For separately acquired MR and PET images, registration was processed using SPM software (Statistical Parametric Mapping, SPM12). The details of the in-house software program are described below.

1. Tumor perfusion parameters from DCE-MRI

1) Pre-processing of T1 signals in DCE-MRI

Baseline T1 signal was measured using pre-T1 images acquired at four different flip angles. Three-dimensional (3D) $R1_0$ and S_0 maps were calculated based on the Ernst formula (TE $\ll$ T2*) using four sets of GRE images with different flip angles:

$$S = \frac{S_0\left(1-\exp\left(-TR/T_{10}\right)\right)\sin\theta}{1-\exp\left(-TR/T_{10}\right)\cos\theta}$$

where "α" has four discrete values in this study (α = 2°, 5°, 10°, and 15°). A linear least square method was used for calculation of the 3D $R1_0$ and S_0 maps (22).

2) Estimation of contrast agent concentration time curves

Four-dimensional (4D; x, y, z, t) post-injection longitudinal

relaxation rate (R1(t)) maps were calculated for each dynamic phase using signal intensity data from the pre- and post-contrast T1W-GRE dynamic series:

$$R1(t) = -(1/TR) \times \ln \frac{1-(A+B)}{1-\cos\theta \times (A+B)}$$

where α = 11° ; TR = 3.5 seconds; $A = \frac{S(t)-S(0)}{S_0 \sin\theta}$; $B = \frac{1-E_{10}}{1-\cos\theta \cdot E_{10}}$; $E_{10} = \exp(-TR \times R_{10})$; and S(0) and S(t) are the signal intensities of images in the 4D T1W-GRE dynamic series before and after contrast injection. 4D gadoterate meglumine concentration maps (x, y, z, t) in tissues [$C_t(t)$] were calculated from 4D $R_1(t)$ maps as follows:

$$R_1(t) = R_{10} + r_1 \times C_t(t)$$

where r_1 is the experimentally determined relaxivity of gadoterate meglumine and r_1 = 4.5mM^{-1}s^{-1} (at 37℃).

3) Determination of individual AIF

For each patient, concentration maps in blood ($C_b(t)$ maps) were calculated based on the ROI in the left ventricle. Concentration maps in the plasma ($C_p(t)$ maps) were calculated from $C_b(t)$ maps using the following equation, where hematocrit (Hct) was 0.4:

$$C_p(t) = \frac{C_b(t)}{1-Hct}$$

4) Parameter estimation for a given compartmental model

3D perfusion parameter (K_{trans}) maps were calculated from the $C_p(t)$ and 4D $C(t)$ maps using the single-tissue compartment modified Tofts model:

$$C_t(t) = K_{trans}\int_0^t C_p(u)\cdot e^{-(K_{trans}/V_e)(t-u)}du + v_p C_p(t)$$

2. Tumor perfusion parameters from $^{13}N-NH_3$ PET

Perfusion parameters from $^{13}N-NH_3$ PET were calculated using several different methods. First, they were quantified using a 2-tissue (2TCM) or 1-tissue (1TCM) compartment model. Goodness-of-fit factors (the Akaike information criteria [AIC], Schwartz criteria [SC], and model selection [MSC] criteria) were calculated for comparison of 1TCM and 2TCM perfusion parameters. Second, at the ROI-level, perfusion parameters were estimated from a single time-activity curve (TAC) of ROI or by averaging the parameters of voxels within the ROI.

1) Two-tissue compartment model (2TCM)

As in the equation for DCE-MRI parameters, $C_a(t)$ is the concentration of $^{13}N-$ NH_3 in arterial blood and $C_t(t)$ is the concentration of tracer in tissues. This model, which assumes that ^{13}N in tissue is in a freely diffusible (C_e) (intra- and extravascular) or a metabolically trapped (C_m) state, can be expressed as:

$$C_t(t) = C_e(t) + C_m(t) = \frac{K_1}{k_2 + k_3} C_a(t) \times [k_3 + k_2 e^{-(k_2+k_3)t}]$$

Since the rate of diffusion of $^{13}N-NH_3$ across the capillary wall is high, the rate constant K_1 is an indicator of blood flow. To address the issues of spillover and partial-volume recovery, it was assumed that

$$\bar{C}_t(t) = (1 - V_a) \cdot C_t(t) + V_a \cdot C_a(t)$$

where $\bar{C}_t(t)$ is the concentration of tracer in tissues; V_a is a real number between 0 and 1; and $(1 - V_a)$ is a regional estimate of the tissue partial-volume recovery coefficient. $^{13}N-NH_3$ PET perfusion parameters (K_1) were estimated using a generalized linear least square method (23).

2) One-tissue compartment model (1TCM)

This model assumes that ^{13}N is present either in blood (C_a) or in tissues (C_t) and can be expressed as:

$$\frac{dC_t(t)}{dt} = K_1 C_a(t) - k_2 C_t(t)$$

Using this model, $^{13}N-NH_3$ PET perfusion parameters (K_1, k_2) were estimated using the linear least square method.

3. Voxel-matching of parametric maps from DCE-MRI and $^{13}N-NH_3$ PET

The voxel resolutions of DCE-MRI and $^{13}N-NH_3$ PET were 1.03 × 1.03 × 3 mm and 1.4 × 1.4 × 1.4 mm, respectively. For voxel-wise comparison of K_{trans} and K_1, parametric map images from PET (K_1 map) were re-sliced into the same resolution as those from DCE-MRI (K_{trans} map) using SPM software. Thus, the TACs and input functions for both PET and MR images could be obtained at each tumor voxel using the same masking image.

Objectives and Outcomes

Primary objective was to compare the regression function between the simultaneous versus separate acquisition. Secondary objective was 1) to measure the correlation coefficients between K_{trans} and K_1, 2) to measure reproducibility of K_{trans} and K_1, 3) to explain the regression function of K_{trans} and K_1 from simultaneous imaging, and 4) to compare 1TCM vs 2TCM in quantitative measurement of tumor perfusion parameters from $^{13}N-NH_3$ PET.

Primary outcome was the regression function of K_{trans} and K_1. Secondary outcomes were Pearson's correlation coefficients between K_{trans} and K_1, intra-class correlation coefficients (ICC) of K_{trans} and K_1 and Goodness-of-fit factors (the AIC, SC, and MSC criteria).

Radiation Protection

All efforts were made to minimize radiation exposure during the experiments, by using MR-compatible syringe shield and by maintaining the distance from animals and ammonia syringes as far as possible. To maintain consistent injection rate of MR and PET contrast media and to minimize radiation exposure, injection through contrast media injector is better than manual injection. However, there has been no available commercial dual injector than can be used for MR/PET. Therefore, a study investigator (K.H.L.) had to manually inject MR and contrast media. Research assistants were also aware of radiation exposure while transporting the animals from MR/PET room to the waiting room, and tried to minimize radiation exposure by keeping the distance from animals and ammonia syringes as far as possible after transportation.

Statistical Analyses

Pearson's correlation coefficients between K_{trans} and K_1 were calculated. The adjusted correlation coefficients were calculated in ROI- and voxel-level by the method of Bland and Altman (24, 25) which accounts for the lack of independence among repeated measurements. Correlation coefficients were interpreted

as follows; 0–0.3, negligible; 0.3–0.5, low positive; 0.5–0.7, moderate positive; 0.7–0.9, high positive; and 0.9–1.0, very high positive correlation (26). The relationship between K_{trans} and K_1 on ROI-level was analyzed using a linear/nonlinear regression function. Reproducibility of K_{trans} and K_1 between two successive days on ROI-level were estimated using ICC by two-way mixed-effects analysis, and ICCs of individual consistency-of-agreement were interpreted as follows; 0–0.2, poor; 0.2–0.4, fair; 0.4–0.6, moderate; 0.6–0.8, good; and 0.8–1.0, excellent correlation. Data analyses were performed using the Stata software package (version 14; Stata, College Station, Tex).

RESULTS

On ultrasonography, successful growth of VX2 tumors was confirmed in all eight rabbits, one week after tumor implantation (**Figure 2**). Therefore, all eight rabbits underwent MR/PET examination, 14 days after tumor implantation. Of the eight rabbits, one died from air-embolism during the 10-min dynamic MR/PET examination. The remaining seven rabbits successfully underwent MR/PET and were sacrificed after the second MR/PET imaging session by intravenous injection of 5 ml potassium chloride while

under deep anesthesia. Because of some error in storage of the raw data of two rabbits, the final analysis included only five rabbits. Representative MR/PET images from simultaneous and separate MR/PET acquisition are shown in Figure 3.

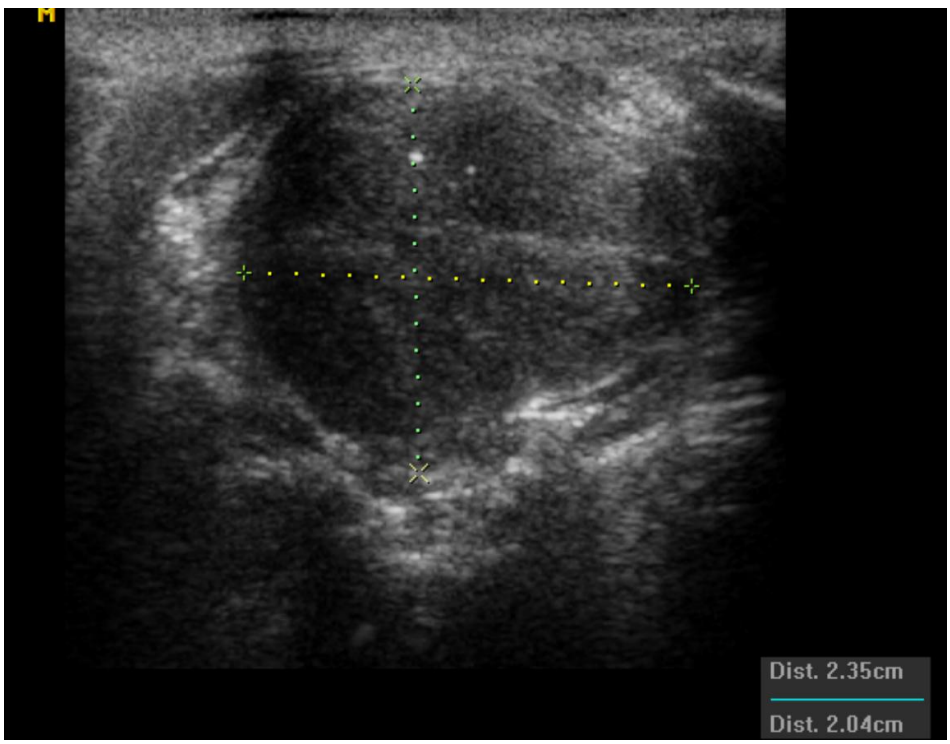

Figure 2. An example of the ultrasonographic images.

To examine rabbits in which tumor implantation was successful, ultrasonographic examination was done to confirm tumor growth one week after tumor implantation.

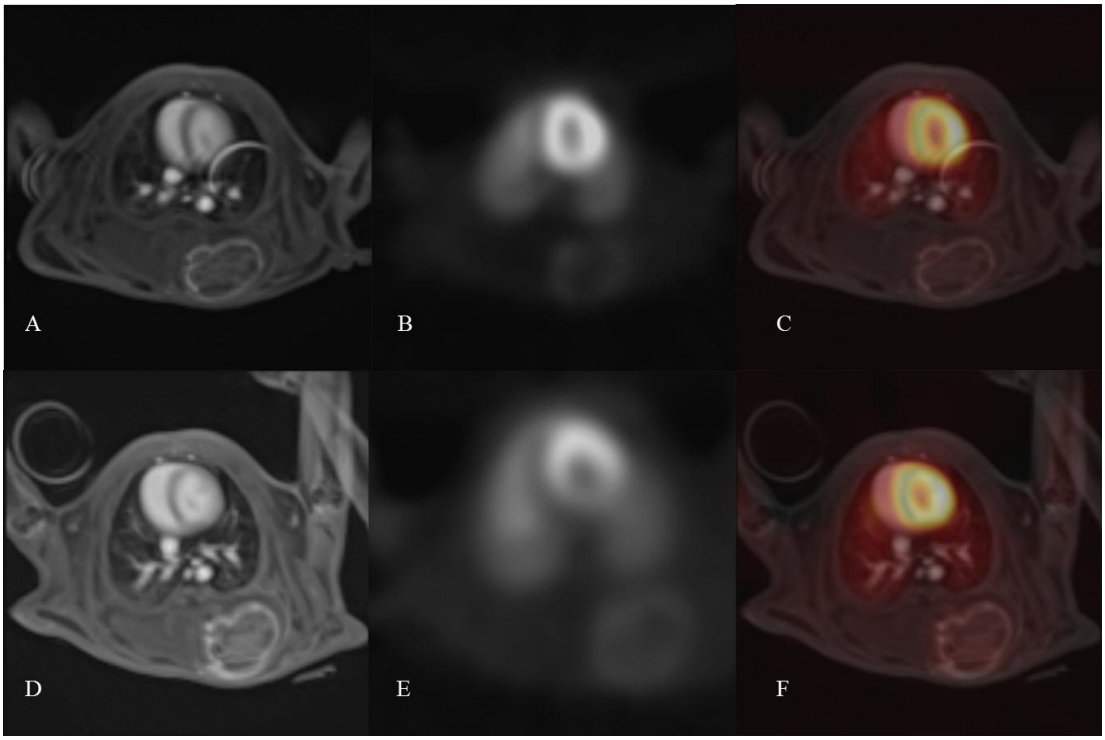

Figure 3. An example of the MR and PET images.

(A) Dynamic contrast-enhanced MR, (B) Dynamic $^{13}N-NH_3$ PET, and (C) Fused MR/PET images with simultaneous MR/PET acquisition 14 days after tumor implantation.

(D) Dynamic contrast-enhanced MR, (E) Dynamic $^{13}N-NH_3$ PET, and (F) Fused MR/PET images with separate MR and PET acquisition at 15 days after tumor implantation.

Rabbit tumor characteristics

VX2 tumors were successfully grown in all five rabbits. The long diameters of the tumors ranged from 2.3−2.9 cm (**Table 1**). The size of whole tumor, that of necrotic area, and the proportion of necrotic area was similar between the day 14 and day 15 (**Table 2**). The number of ROIs outlining the tumors ranged from 12 to 18 per rabbit (total, 71 ROIs). K_{trans} and K_1 values of tumors were calculated successfully using in−house software program. Representative arterial input function curves and parametric maps are shown in **Figure 4**. The mean ± standard deviation of K_{trans} was 0.062 ± 0.04 min^{-1} and 0.036 ± 0.02 min^{-1}, with simultaneous and separate image acquisition, respectively. The mean ± standard deviation of K_1 calculated by 1TCM was 0.339 ± 0.11 mL/min/g and 0.231 ± 0.16 mL/min/g, with simultaneous and separate image acquisition, respectively. The mean ± standard deviation of K_1 calculated by 2TCM was 0.365 ± 0.12 mL/min/g and 0.224 ± 0.15 mL/min/g, with simultaneous and separate image acquisition, respectively.

Table 1. Summary of tumor characteristics in five rabbits

Rabbit			1	2	3	4	5
Tumor size	Long x short diameter (cm)		2.6 x 2.0	2.6 x 1.8	2.6 x 1.9	2.3 x 2.0	2.9 x 2.6
Simultaneous scan	MR	K_{trans} [min^{-1}]	0.027 ± 0.02	0.046 ± 0.04	0.038 ± 0.03	0.072 ± 0.05	0.128 ± 0.14
		k_{ep} [min^{-1}]	0.142 ± 0.01	0.159 ± 0.01	0.168 ± 0.02	0.228 ± 0.02	0.280 ± 0.02
	PET	K_1 (1TCM) [mL/min/g]	0.209 ± 0.11	0.301 ± 0.15	0.346 ± 0.19	0.442 ± 0.19	0.389 ± 0.20
		k_2 (1TCM) [min^{-1}]	0.475 ± 0.04	0.997 ± 0.10	1.147 ± 0.25	1.322 ± 0.18	1.178 ± 0.22
		K_1 (2TCM) [mL/min/g]	0.245 ± 0.12	0.285 ± 0.13	0.367 ± 0.17	0.479 ± 0.18	0.433 ± 0.20
Separate scan	MR	K_{trans} [min^{-1}]	0.024 ± 0.09	0.043 ± 0.06	0.033 ± 0.03	0.040 ± 0.06	0.042 ± 0.04
		k_{ep} [min^{-1}]	0.045 ± 0.04	0.180 ± 0.04	0.168 ± 0.03	0.308 ± 0.04	0.132 ± 0.03
	PET	K_1 (1TCM) [mL/min/g]	0.087 ± 0.05	0.157 ± 0.13	0.450 ± 0.17	0.160 ± 0.09	0.287 ± 0.14
		k_2 (1TCM) [min^{-1}]	0.436 ± 0.03	0.728 ± 0.14	1.467 ± 0.17	0.522 ± 0.10	0.970 ± 0.15
		K_1 (2TCM) [mL/min/g]	0.100 ± 0.06	0.162 ± 0.13	0.433 ± 0.18	0.195 ± 0.12	0.285 ± 0.14

1TCM, 1−tissue compartment model

2TCM, 2−tissue compartment model

Data are presented as mean ± standard deviation.

Table 2. Size of the whole tumor and necrotic area with the simultaneous and separate image acquisition in five rabbits

Rabbit No.	Tumor size (mm)	Necrotic area size (mm)	Necrotic area proportion (%)	Protocol
1	28	23	82	Simultaneous
	27	23	85	Separate
2	30	27	90	Simultaneous
	31	28	90	Separate
3	28	26	93	Simultaneous
	30	26	87	Separate
4	25	21	84	Simultaneous
	27	22	81	Separate
5	31	27	87	Simultaneous
	32	27	84	Separate

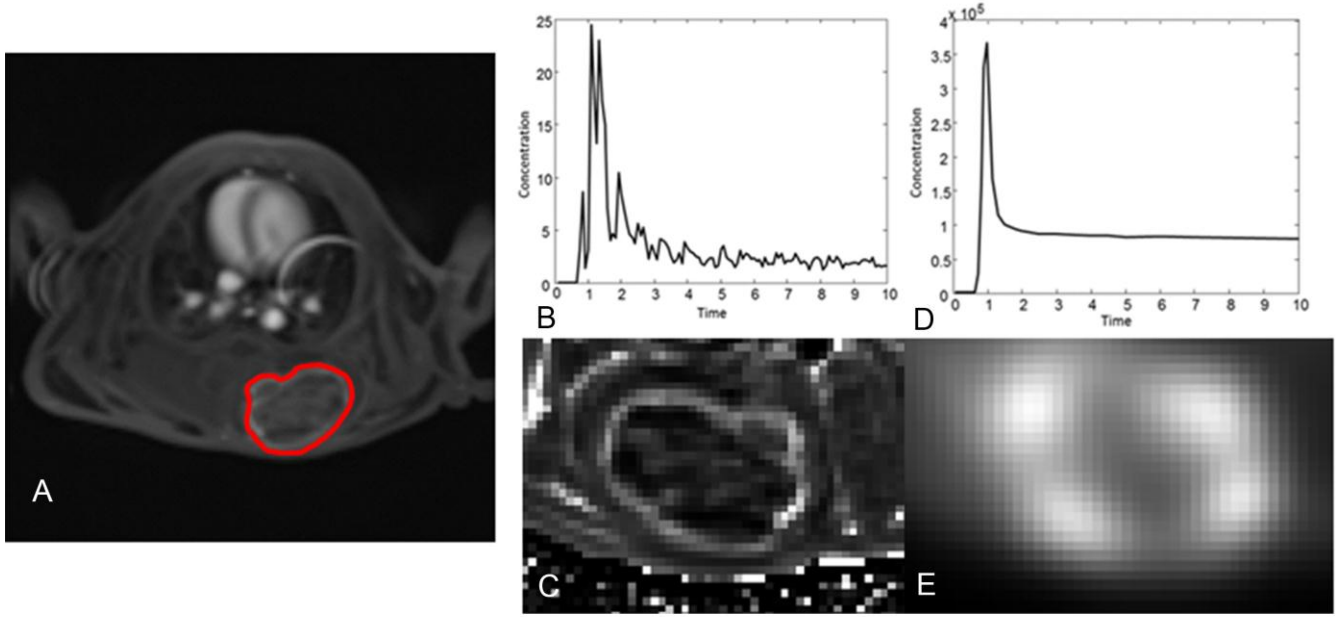

Figure 4. Parameteric maps of K_{trans} and K_1.

(A) An representative ROI outlining the entire tumor boundary drawn by a board-certified radiologist on dynamic contrast-enhanced MRI.

(B) Arterial input function curve and (C) K_{trans} map from dynamic contrast-enhanced MRI.

(D) Arterial input function curve and (E) K_1 map from dynamic $^{13}N-NH_3$ PET using 1-tissue compartment model.

Dynamic NH_3 PET Modeling

The AIC, SC, and MSC values of 1TCM and 2TCM are shown in Table 3. The 1TCM model was found to be more appropriate model, given its lower AIC and SC values and greater MSC values in comparison with those of the 2TCM model.

Table 3. Goodness-of-fit parameters of the 1-tissue compartment model (1TCM) and 2-tissue compartment model (2TCM) in ^{13}N-NH_3 PET

	1TCM	2TCM
Simultaneous scan		
AIC	382.0 ± 10.9	400.4 ± 40.4
SC	386.0 ± 10.9	405.6 ± 40.4
MSC	4.7 ± 0.4	4.1 ± 1.5
Separate scan		
AIC	380.0 ± 33.9	397.7 ± 57.6
SC	384.2 ± 33.9	402.9 ± 57.6
MSC	5.2 ± 1.0	4.6 ± 1.5

AIC, Akaike information

SC, Schwartz criteria

MSC, model selection criteria

Data are presented as mean ± standard deviation.

Correlation coefficients between K_{trans} and K_1

Assuming a linear relationship, there was a positive correlation between MR (K_{trans}) and PET (K_1) perfusion parameters at the ROI- and voxel-levels (**Table 4**). At the ROI-level, MR and PET perfusion parameters exhibited moderate positive correlations with simultaneous (r = 0.54-0.57) and separate (r = 0.53-0.69) imaging. At the voxel-level, the two sets of parameters exhibited only negligible correlations with simultaneous (r = 0.24) and separate (r = 0.16-0.18) imaging.

Table 4. Correlation coefficient between K_{trans} and K_1 with simultaneous scan and separate scan

	Simultaneous scan	Separate scan
Voxel-level analysis		
1TCM	0.24	0.18
2TCM	0.24	0.16
ROI-level analysis		
Average of voxel parameters, 1TCM	0.55	0.65
Average of voxel parameters, 2TCM	0.57	0.58
Single TAC, 1TCM	0.54	0.69
Single TAC, 2TCM	0.56	0.53

1TCM, 1-tissue compartment model

2TCM, 2-tissue compartment model

TAC, time-activity curve

Relationship between K_{trans} and K_1

While the K_{trans} and K_1 from separate imaging exhibited a linear relationship, those from simultaneous imaging exhibited a nonlinear relationship (**Figures 5, 6**).

The regression function which fitted in the scatterplot of the K_{trans} and K_1 obtained from simultaneous imaging was as follows, even though the value of R-squared was not fairly high. With simultaneous imaging, the amount of change in K_1 associated with a unit increase in K_{trans} varied depending on the values of K_{trans}.

1) 1TCM

$$K_1 = 0.1279 * \ln (K_{trans}) + 0.7166, \text{R-squared: } 0.4342$$

2) 2TCM

$$K_1 = 0.1421 * \ln (K_{trans}) + 0.7841, \text{R-squared: } 0.4676$$

The regression function which fitted in the scatterplot of the K_{trans} and K_1 obtained from simultaneous imaging was as follows, even though the value of R-squared was relatively small. With separate imaging, the amount of change in K_1 associated with a unit increase in K_{trans} did not vary depending on the values of K_{trans}.

1) 1TCM

$K_1 = 4.8089 * K_{trans} + 0.0568$, R-squared: 0.2321

2) 2TCM

$K_1 = 4.8269 * K_{trans} + 0.0491$, R-squared: 0.2617

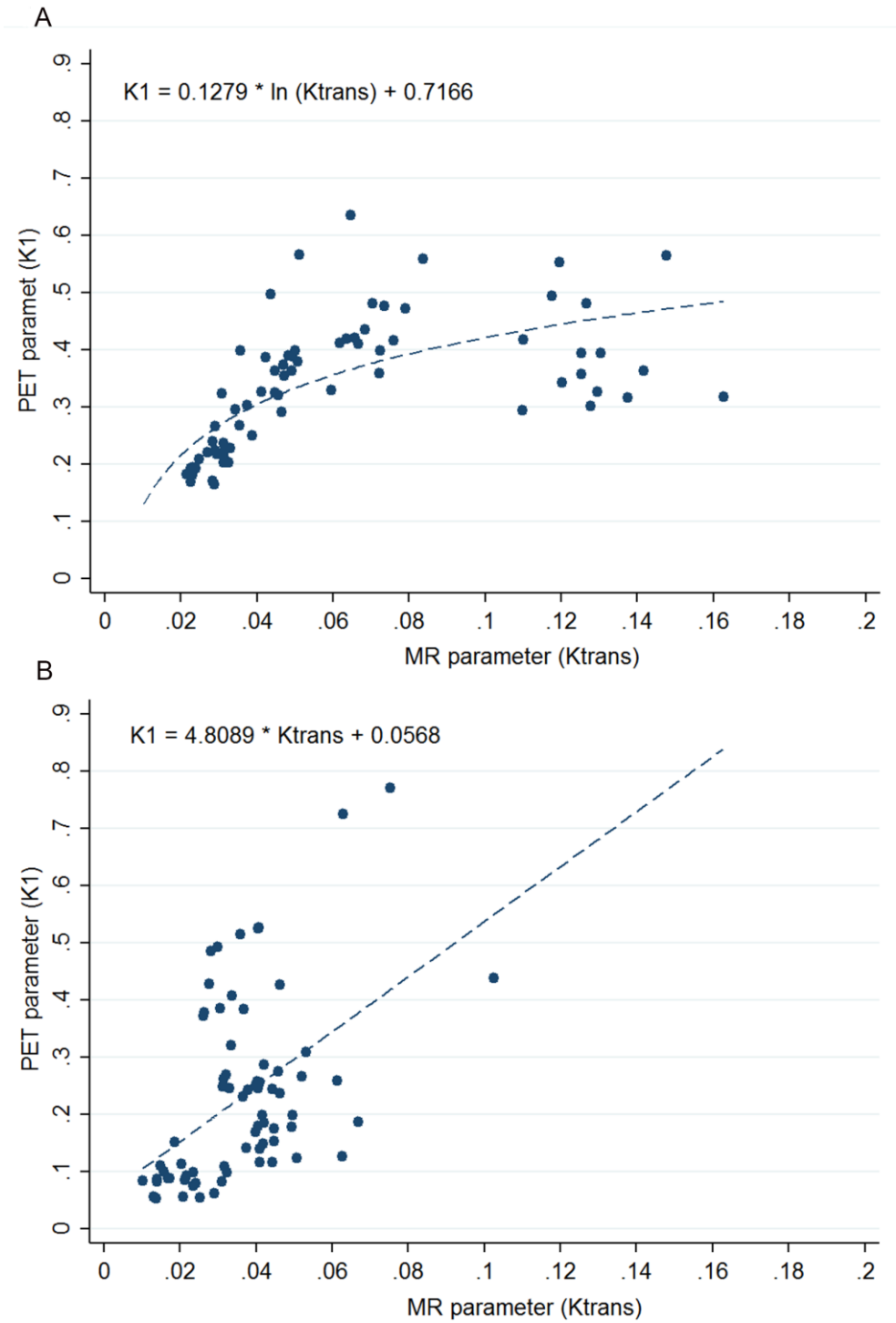
A
K1 = 0.1279 * ln (Ktrans) + 0.7166
PET paramet (K1)
0
.1
.2
.3
.4
.5
.6
.7
.8
.9
0
.02
.04
.06
.08
.1
.12
.14
.16
.18
.2
MR parameter (Ktrans)
B
K1 = 4.8089 * Ktrans + 0.0568
PET parameter (K1)
0
.1
.2
.3
.4
.5
.6
.7
.8
.9
0
.02
.04
.06
.08
.1
.12
.14
.16
.18
.2
MR parameter (Ktrans)

Figure 5. Scatterplot of K_{trans} versus K_1 (K_1 was calculated using 1TCM).

(A) K_{trans} versus K_1 from simultaneous MR/PET acquisition

(B) K_{trans} versus K_1 from separate MR and PET acquisition.

In each plot, a yellow line represents an equation estimated from a regression function.

A

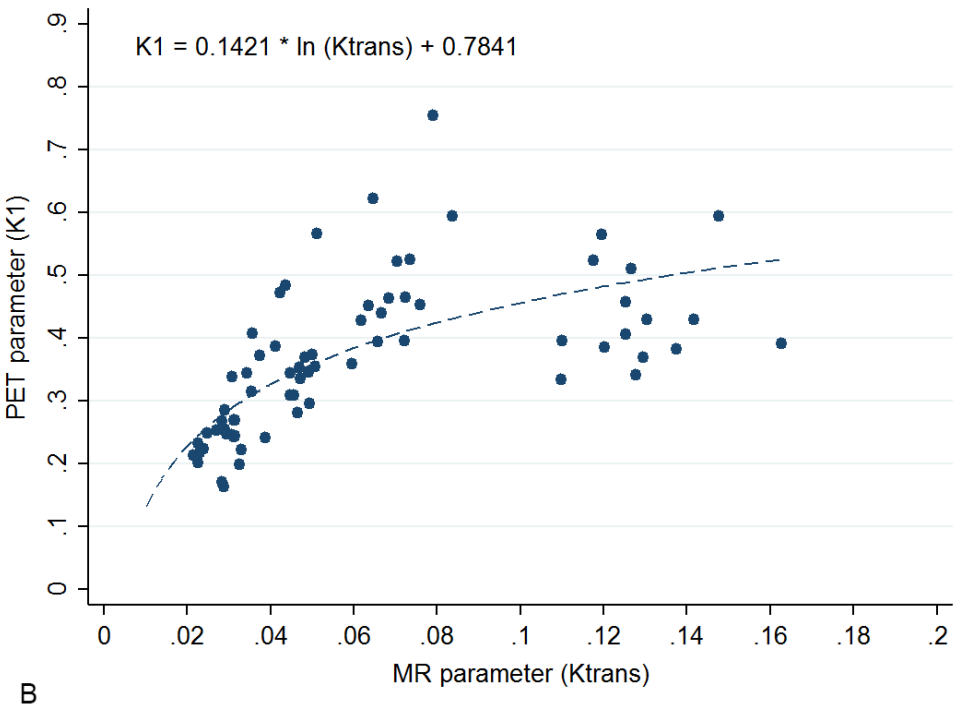
K1 = 0.1421 * ln (Ktrans) + 0.7841
PET parameter (K1)
0
.1
.2
.3
.4
.5
.6
.7
.8
.9
0
.02
.04
.06
.08
.1
.12
.14
.16
.18
.2
MR parameter (Ktrans)

B

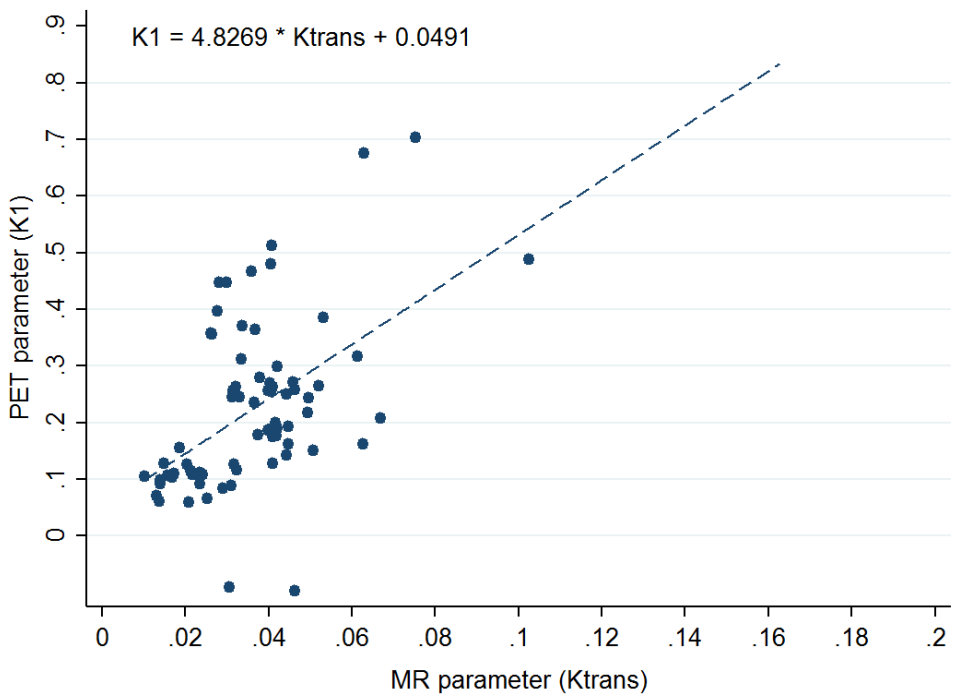
K1 = 4.8269 * Ktrans + 0.0491
PET parameter (K1)
0
.1
.2
.3
.4
.5
.6
.7
.8
.9
0
.02
.04
.06
.08
.1
.12
.14
.16
.18
.2
MR parameter (Ktrans)

Figure 6. Scatterplot of K_{trans} versus K_1 (K_1 was calculated using 2TCM).

(A) K_{trans} versus K_1 from simultaneous MR/PET acquisition

(B) K_{trans} versus K_1 from separate MR and PET acquisition.

In each plot, a yellow line represents an equation estimated from a regression function.

Reproducibility of K_{trans} and K_1

While the ICCs of K_{trans} between simultaneous and separate imaging revealed fair agreement (ICC, 0.29–0.31), those of K_1 demonstrated moderate agreement (ICC, 0.44–0.49) (Table 5).

Table 5. Reproducibility of K_{trans} and K_1 on ROI-level between two successive days

	K_{trans} [min^{-1}]	K_1 [mL/min/g]
Average of voxel parameters, 1TCM	0.29	0.46
Average of voxel parameters, 2TCM	0.29	0.49
Single TAC, 1TCM	0.31	0.44
Single TAC, 2TCM	0.31	0.44

1TCM, 1-tissue compartment model

2TCM, 2-tissue compartment model

TAC, time-activity curve

DISCUSSION

In this study, K_{trans} and K_1 exhibited moderate positive correlations with both simultaneous (r = 0.54–0.57) and separate (r = 0.53–0.69) imaging at the ROI-level, under the assumption of linear relationship between MR and PET parameters, as demonstrated with separate image acquisition. However, careful examination of the association between MR and PET parameters from simultaneous imaging revealed a nonlinear relationship between K_{trans} and K_1. The amount of change in K_1 associated with a unit increase in K_{trans} varied depending on the values of K_{trans}.

With simultaneous MR/PET examination, more robust investigation of the relationship between MR and PET perfusion parameters is possible than with separate acquisition. Simultaneity is one of the most powerful merits of hybrid MR/PET imaging in comparison with separate PET and MRI or PET/CT, which involves CT followed by PET, hoping that the subject does not move between the two procedures. However, hybrid MR/PET has not been thoroughly investigated, especially in terms of its ability to acquire in-vivo functional information, although its necessity has been recently suggested (3, 27). Simultaneous acquisition not only saves time but also enables better alignment quality (7) and precise

evaluation of the relationship between MR and PET parameters under identical tissue microenvironments.

Validation of CT and MRI perfusion parameters has been performed mostly in brain and myocardial imaging (28, 29). Unlike perfusion imaging of the myocardium or the brain, there has been no established gold standard imaging method for tumor perfusion because of the possibility of tissue-dependent pathologic vascular abnormalities, such as vascular leakage, shunting, or malformation (30, 31). Instead, validation against histopathological findings such as microvessel density or vascular endothelial growth factors has been attempted for some tumors; however, the results were inconsistent and did not accurately reflect true tumor perfusion in vivo (32, 33). Furthermore, pathologic perfusion markers do not reflect perfusion in vivo. Therefore, investigation of the relationship between perfusion parameters from two different imaging modalities might serve to cross-validate each parameter. The present results indicate that K_{trans} demonstrates a fair amount of blood flow, which is represented by K_1. However, the amount of change in K_1 associated with a unit increase in K_{trans} was not always the same with simultaneous MR/PET acquisition, probably because K_{trans} is influenced by both blood flow and permeability. Assuming the simple linear correlation between K_{trans} and K_1 based solely on

separate MR and PET images might result in misinterpretation of the relationship between the two sets of parameters. In our study, voxel-level analysis revealed only the negligible correlation between the two parameters. The limited resolution and blurring of PET images might explain this weak correlation on voxel-level and discrepancy between the voxel- and ROI-level analysis.

While $^{13}N-NH_3$ PET has been used in myocardial perfusion imaging, only a few studies have examined its utility in tumor imaging (15-18). Prior studies have demonstrated that $^{13}N-NH_3$ PET might be a useful imaging tool for semi-quantitative evaluation of tumor perfusion (15-17). Since this is the first study involving quantitative dynamic $^{13}N-NH_3$ PET in tumor imaging, we estimated perfusion parameters using two different tissue-compartment models. Although the 2TCM has been widely used in myocardial perfusion, our data indicated that the 1TCM was more appropriate for tumor imaging. This difference might be attributable to the faster circulation time of rabbits, differences in microenvironments, and vascular abnormalities within the tumor.

In the present study, the values of K_1 (ICC, 0.44-0.49) were more reproducible than those of K_{trans} (ICC, 0.29-0.31). Nonetheless, the overall reproducibility of K_1 and K_{trans} in this study was relatively low when compared to those reported in several

previous studies (34-36). Since the reproducibility of perfusion parameters may vary according to the calculation method (37, 38), we speculate that the low reproducibility observed in the present study could be associated with several factors including the one-day gap between simultaneous and separate imaging, calculation of pre-T1 values, estimation of individual AIF or TACs, and manual contrast media injection. Indeed, recent studies have also demonstrated the low reproducibility of perfusion parameters which is comparable to our study (39, 40).

There are some limitations to the present study. First, this study included a small number of rabbits. Second, we chose ^{13}N-NH_3 as a perfusion marker instead of $^{15}H_2O$, which is regarded as the gold standard for in vivo estimation of perfusion in the myocardium and brain, for the following reasons: (a) in comparison $^{15}H_2O$, the longer half-life of ^{13}N-NH_3 (10 min) enables more consistent radiotracer injection among the subjects; (b) the main purpose of this study was to compare simultaneous and separate MR/PET, rather than validation of DCE-MRI, and (c) ^{13}N-NH_3 PET has been under-investigated as a tumor perfusion marker. Third, only quantitative perfusion parameters of MR and PET were evaluated in this study. Due to the limited reproducibility of quantitative perfusion parameters, semiquantitative parameters

such as initial area under the gadolinium concentration-time curve might have provided additional information. Fourth, temporal resolution of 5 second was relatively slow to evaluate the perfusion parameters of small animals. Finally, since the volume of blood flow and permeability might vary among tumors, the relationship between K_1 and K_{trans} might also vary among different tumors.

In conclusion, the relationship between K_{trans} and K_1 was different between simultaneous and separate MR/PET acquisition. The relationship between K_{trans} and K_1 may be mis-interpreted with separate MR and PET acquisition.

REFERENCES

1. Torigian DA, Zaidi H, Kwee TC, et al. PET/MR imaging: technical aspects and potential clinical applications. *Radiology*. 2013;267(1):26-44.

2. Yoo HJ, Lee JS, Lee JM. Integrated whole body MR/PET: where are we? *Korean J Radiol*. 2015;16(1):32-49.

3. Yoon SH, Goo JM, Lee SM, Park CM, Seo HJ, Cheon GJ. Positron emission tomography/magnetic resonance imaging evaluation of lung cancer: current status and future prospects. *J Thorac Imaging*. 2014;29(1):4-16.

4. Chandarana H, Heacock L, Rakheja R, et al. Pulmonary nodules in patients with primary malignancy: comparison of hybrid PET/MR and PET/CT imaging. *Radiology*. 2013;268(3):874-881.

5. Eiber M, Takei T, Souvatzoglou M, et al. Performance of whole-body integrated 18F-FDG PET/MR in comparison to PET/CT for evaluation of malignant bone lesions. *J Nucl Med*. 2014;55(2):191-197.

6. Bailey DL, Antoch G, Bartenstein P, et al. Combined PET/MR: The Real Work Has Just Started. Summary Report of the Third International Workshop on PET/MR Imaging; February 17-21, 2014, Tubingen, Germany. *Mol Imaging Biol*. 2015;17(3):297-312.

7. Brendle CB, Schmidt H, Fleischer S, Braeuning UH, Pfannenberg CA, Schwenzer NF. Simultaneously acquired MR/PET images compared with sequential MR/PET and PET/CT: alignment quality. *Radiology*. 2013;268(1):190-199.

8. Nielsen T, Wittenborn T, Horsman MR. Dynamic Contrast-Enhanced Magnetic Resonance Imaging (DCE-MRI) in Preclinical Studies of Antivascular Treatments. *Pharmaceutics*. 2012;4(4):563-589.

9. Padhani AR. Dynamic contrast-enhanced MRI in clinical oncology: current status and future directions. *J Magn Reson Imaging*. 2002;16(4):407-422.

10. Komori T, Narabayashi I, Matsumura K, et al. 2-[Fluorine-18]-fluoro-2-deoxy-D-glucose positron emission tomography/computed tomography versus whole-body diffusion-weighted MRI for detection of malignant lesions: initial experience. *Ann Nucl Med*. 2007;21(4):209-215.

11. Cuenod CA, Fournier L, Balvay D, Guinebretiere JM. Tumor angiogenesis: pathophysiology and implications for contrast-enhanced MRI and CT assessment. *Abdom Imaging*. 2006;31(2):188-193.

12. Schepis T, Gaemperli O, Treyer V, et al. Absolute quantification of myocardial blood flow with 13N-ammonia and 3-dimensional

PET. *J Nucl Med*. 2007;48(11):1783-1789.

13. Slomka PJ, Alexanderson E, Jacome R, et al. Comparison of clinical tools for measurements of regional stress and rest myocardial blood flow assessed with 13N-ammonia PET/CT. *J Nucl Med*. 2012;53(2):171-181.

14. Eby PR, Partridge SC, White SW, et al. Metabolic and vascular features of dynamic contrast-enhanced breast magnetic resonance imaging and (15)O-water positron emission tomography blood flow in breast cancer. *Acad Radiol*. 2008;15(10):1246-1254.

15. Xiangsong Z, Weian C. Differentiation of recurrent astrocytoma from radiation necrosis: a pilot study with 13N-NH3 PET. *J Neurooncol*. 2007;82(3):305-311.

16. Khangembam BC, Karunanithi S, Sharma P, et al. Perfusion-metabolism coupling in recurrent gliomas: a prospective validation study with 13N-ammonia and 18F-fluorodeoxyglucose PET/CT. *Neuroradiology*. 2014;56(10):893-902.

17. Xiangsong Z, Changhong L, Weian C, Dong Z. PET Imaging of cerebral astrocytoma with 13N-ammonia. *J Neurooncol*. 2006;78(2):145-151.

18. Harisankar CN, Mittal BR, Watts A, Bhattacharya A, Sen R. Utility of dynamic perfusion PET using (1)(3)N-ammonia in diagnosis of asymptomatic recurrence of fibrosarcoma. *Clin Nucl*

Med. 2011;36(2):150-151.

19. Rivera B, Ahrar K, Kangasniemi MM, Hazle JD, Price RE. Canine transmissible venereal tumor: a large-animal transplantable tumor model. *Comp Med*. 2005;55(4):335-343.

20. Joo I, Lee JM, Grimm R, Han JK, Choi BI. Monitoring Vascular Disrupting Therapy in a Rabbit Liver Tumor Model: Relationship between Tumor Perfusion Parameters at IVIM Diffusion-weighted MR Imaging and Those at Dynamic Contrast-enhanced MR Imaging. *Radiology*. 2016;278(1):104-113.

21. Park HS, Han JK, Lee JM, et al. Dynamic Contrast-Enhanced MRI Using a Macromolecular MR Contrast Agent (P792): Evaluation of Antivascular Drug Effect in a Rabbit VX2 Liver Tumor Model. *Korean J Radiol*. 2015;16(5):1029-1037.

22. Murase K. Efficient method for calculating kinetic parameters using T1-weighted dynamic contrast-enhanced magnetic resonance imaging. *Magn Reson Med*. 2004;51(4):858-862.

23. Feng D, Huang SC, Wang ZZ, Ho D. An unbiased parametric imaging algorithm for nonuniformly sampled biomedical system parameter estimation. *IEEE Trans Med Imaging*. 1996;15(4):512-518.

24. Bland JM, Altman DG. Calculating correlation coefficients with repeated observations: Part 1--Correlation within subjects. *BMJ*.

1995;310(6977):446.

25. Bland JM, Altman DG. Correlation, regression, and repeated data. *BMJ*. 1994;308(6933):896.

26. Mukaka MM. Statistics corner: A guide to appropriate use of correlation coefficient in medical research. *Malawi Med J*. 2012;24(3):69-71.

27. Bailey DL, Barthel H, Beuthin-Baumann B, et al. Combined PET/MR: Where are we now? Summary report of the second international workshop on PET/MR imaging April 8-12, 2013, Tubingen, Germany. *Mol Imaging Biol*. 2014;16(3):295-310.

28. Raichle ME, Martin WR, Herscovitch P, Mintun MA, Markham J. Brain blood flow measured with intravenous H2(15)O. II. Implementation and validation. *J Nucl Med*. 1983;24(9):790-798.

29. Bergmann SR, Fox KA, Rand AL, et al. Quantification of regional myocardial blood flow in vivo with H215O. *Circulation*. 1984;70(4):724-733.

30. Brix G, Griebel J, Kiessling F, Wenz F. Tracer kinetic modelling of tumour angiogenesis based on dynamic contrast-enhanced CT and MRI measurements. *Eur J Nucl Med Mol Imaging*. 2010;37 Suppl 1:S30-51.

31. Jeswani T, Padhani AR. Imaging tumour angiogenesis. *Cancer Imaging*. 2005;5:131-138.

32. Hulka CA, Edmister WB, Smith BL, et al. Dynamic echo-planar imaging of the breast: experience in diagnosing breast carcinoma and correlation with tumor angiogenesis. *Radiology*. 1997;205(3):837-842.

33. Su MY, Cheung YC, Fruehauf JP, et al. Correlation of dynamic contrast enhancement MRI parameters with microvessel density and VEGF for assessment of angiogenesis in breast cancer. *J Magn Reson Imaging*. 2003;18(4):467-477.

34. Ferrier MC, Sarin H, Fung SH, et al. Validation of dynamic contrast-enhanced magnetic resonance imaging-derived vascular permeability measurements using quantitative autoradiography in the RG2 rat brain tumor model. *Neoplasia*. 2007;9(7):546-555.

35. Wang H, Su Z, Ye H, et al. Reproducibility of Dynamic Contrast-Enhanced MRI in Renal Cell Carcinoma: A Prospective Analysis on Intra- and Interobserver and Scan-Rescan Performance of Pharmacokinetic Parameters. *Medicine (Baltimore)*. 2015;94(37):e1529.

36. Zhang X, Pagel MD, Baker AF, Gillies RJ. Reproducibility of magnetic resonance perfusion imaging. *PLoS One*. 2014;9(2):e89797.

37. Craciunescu O, Brizel D, Cleland E, et al. Dynamic contrast enhanced-MRI in head and neck cancer patients: variability of the

precontrast longitudinal relaxation time (T10). *Med Phys*. 2010;37(6):2683-2692.

38. Cron GO, Foottit C, Yankeelov TE, Avruch LI, Schweitzer ME, Cameron I. Arterial input functions determined from MR signal magnitude and phase for quantitative dynamic contrast-enhanced MRI in the human pelvis. *Magn Reson Med*. 2011;66(2):498-504.

39. Beuzit L, Eliat PA, Brun V, et al. Dynamic contrast-enhanced MRI: Study of inter-software accuracy and reproducibility using simulated and clinical data. *J Magn Reson Imaging*. 2016;43(6):1288-1300.

40. Heye T, Davenport MS, Horvath JJ, et al. Reproducibility of dynamic contrast-enhanced MR imaging. Part I. Perfusion characteristics in the female pelvis by using multiple computer-aided diagnosis perfusion analysis solutions. *Radiology*. 2013;266(3):801-811.

초 록

서론: 본 연구는 토끼 VX2 종양을 이용하여 역동적 조영 증강 자기공명영상과 역동적 암모니아 양성자방출단층촬영을 동시 촬영했을 때와 분리 촬영했을 때의 K_{trans}과 K_1의 관계를 비교하기 위한 동물 실험 연구임.

방법: 8마리 토끼의 왼쪽 척추인접 근육에 VX2 종양을 심고 2주 후, 이틀에 걸쳐 첫째날은 역동적 조영 증강 자기공명영상과 역동적 암모니아 양성자방출단층촬영을 동시에 촬영하였고 이튿날에는 역동적 조영 증강 자기공명영상과 역동적 암모니아 양성자방출단층촬영을 각각 따로 촬영하였음. 관류지표 분석 프로그램을 자체 개발하여 역동적 조영 증강 자기공명영상으로부터 종양의 K_{trans} 값을, 역동적 암모니아 양성자방출단층촬영으로부터 종양의 K_1값을 계산하였음. K_{trans}과 K_1의 관계를 피어슨 상관 계수와 회귀 함수를 이용하여 분석하였음.

결과: 최종 5마리의 토끼가 분석에 포함되었음. K_{trans}과 K_1이 선형 상관관계를 갖는다고 가정하면, 동시 촬영했을 때 (피어슨 상관 계수: $r = 0.54–0.57$) 와 분리 촬영했을 때 (피어슨 상관 계수: $r = 0.53–0.69$) 모두에서 K_{trans}과 K_1은 중간 정도의 양의 상관 관계를 보였음. 그러나 회귀 함수를 이용하여 K_{trans}과 K_1의 관계를 분석해 보았을 때, 분리 촬영했을 때는 K_{trans}과 K_1이 선형 상관 관계를 보였지만 동시 촬영했을 때는 K_{trans}과 K_1은 비선형 상관 관계를 보이고 있었음. 동시 촬영시, K_{trans} 의 단위 증가에 따른 K_1 의 변화량은 K_{trans} 값에 따라 달라졌음.

결론: K_{trans}과 K_1 관계는 역동적 조영 증강 자기공명영상과 역동적 암모니아 양성자방출단층촬영을 동시 촬영했을 때와 분리 촬영했을 때 다르게 나타났음. K_{trans}과 K_1 관계는 역동적 조영 증강 자기공명영상과 역동적 암모니아 양성자방출단층촬영의 분리 촬영에만 기반해서는 그릇되게 해석될 수 있음.

주요어: 자기공명영상/양성자방출단층촬영, 역동적 조영 증강 자기공명영상, 역동적 암모니아 양성자방출단층촬영, 관류 지표, 토끼

학 번: 2013-30559